Fusion-fission analysis of $^{12}C + ^{248}Cm$ and $^{16}O + ^{244}Pu$ nuclear reactions across the Coulomb barrier

Vijay,[1] Neha Grover,[2,3,*] Kanishka Sharma,[4] Manjeet Singh Gautam,[5] Manoj K. Sharma,[6] and Rishi Pal Chahal[1]

[1]*Department of Physics, Chaudhary Bansi Lal University, Bhiwani-127021, Haryana, India*

[2]*Department of Physics, Indian Institute of Technology, Ropar, Rupnagar 140001, India*

[3]*Department of Physics, School of Basic Sciences, Manipal University Jaipur, Jaipur, Rajasthan 303007, India*

[4]*School of Vocational Studies and Applied Sciences (SOVSAS), Gautam Buddha University, Greater Noida, India*

[5]*Department of Physics, Government College Alewa, Jind-126102, Haryana, India*

[6]*School of Physics and Materials Science, Thapar Institute of Engineering and Technology, Patiala-147004, India*

(Received 29 November 2021; accepted 17 October 2022; published 21 December 2022)

By using the symmetric-asymmetric Gaussian barrier distribution (SAGBD) model, Wong formula, and coupled channel approach, heavy ion fusion dynamics is investigated for $^{12}C + ^{248}Cm$ and $^{16}O + ^{244}Pu$ reactions at energies lying below and near the Coulomb barrier. Coupling of various channels linked with the structure of participants to the relative motion of the collision partners is done by considering a Gaussian type of weight function in the SAGBD model and cross sections are found to be enhanced relative to the calculations obtained by the simple barrier penetration model. In the SAGBD model, the channel coupling effects are calculated in terms of channel coupling parameter (λ) and percentage reduction in the height of apparent fusion barrier with respect to the Coulomb barrier ($V_{\rm CBRED}$). The channel coupling parameter estimates the cumulative influence of dominant intrinsic channels, which are responsible for the sub-barrier fusion enhancement. The SAGBD calculations appropriately explain the dynamics of $^{12}C + ^{248}Cm$ and $^{16}O + ^{244}Pu$ reactions at energies lying around the Coulomb barrier. The coupled channel analysis of the present reactions is done by using the code CCFULL and the coupled channel calculations unambiguously identify the dominant influences of the rotational states up to 10^+ spin states of the ground state rotational band of target isotopes in both reactions. In addition, the couplings to higher order deformation, such as β_4 for target and low lying quantum states of the projectile, are necessarily required to reproduce the experimental data of $^{12}C + ^{248}Cm$ and $^{16}O + ^{244}Pu$ reactions. Apart from the fusion analysis, the dynamical cluster-decay model (DCM) is applied to understand the fission dynamics of the $^{260}No^*$ nucleus formed via the above-mentioned reactions. The decay study is carried out at the center-of-mass energies spread, $E_{\rm c.m.}$ ($\approx$79 to 109 MeV) by including the quadrupole deformations (β_2) and optimum orientations ($\theta_i^{\rm opt}$) of the decaying fragments. According to the experimental observation, the noncompound nucleus (nCN) fission component competes with the compound nucleus (CN) fission processes. Consequently, the possibility of nCN contribution is also explored in the decay of the $^{260}No^*$ compound nucleus. With an aim to have a comprehensive analysis of CN and nCN fission mechanisms, the role of the center-of-mass energy ($E_{\rm c.m.}$) and angular momentum (ℓ) is explored in terms of various parameters of DCM such as fragmentation potential, preformation probability, barrier modification, etc.

DOI: 10.1103/PhysRevC.106.064609

I. INTRODUCTION

Among the various types of nuclear interactions, the complex and fascinating aspects of fusion reactions have attracted researchers not only for the cause of energy production in the stellar region but also for the formation of new exotic nuclear isotopes. Heavy ion fusion provides useful information regarding the nuclear structure and interaction potential of the colliding nuclei. Hitherto, a lot of experimental and theoretical imperative studies have been done to explore the dynamics of heavy-ion systems [1–5]. At energies much lower than the Coulomb barrier, the possibility of the occurrence of fusion is a difficult job. The phenomenon in which the fusion occurs at below barrier energies is called tunneling [6]. In other words, quantum mechanically, the fusion probability is found to be nonzero in classically forbidden regions and hence is called a quantum tunneling phenomenon. The coupling of internal degrees of freedom with the relative motion of fusing partners plays a major role is enhancing the cross sections over the calculations obtained by the one-dimensional barrier penetration model (BPM) at energies below and near the Coulomb barrier and is termed fusion enhancement [7–9]. These couplings modify the original barrier and split it into more than one barrier of various heights and weights. Different theoretical models have been proposed to explain this enhancement phenomenon [10–12], however, the explanations of a large number of problems related to fusion are still a milestone for researchers working in this domain.

*Corresponding author: nehagrover9823@gmail.com; neha.grover@jaipur.manipal.edu

The amalgamation (fusion) process has gained more attention during the last few decades because of its close alliance with the nucleus-nucleus potential [13,14]. To understand the importance of the interaction potential between fusion pairs, a lot of experimental and theoretical studies have been done on fusion cross sections over the last few decades [1,15–19]. In literature [1–5], for the fusion process, the channel coupling effects were entertained by the nuclear component of the total interaction potential which is mostly described by a standard Woods-Saxon potential. The Woods-Saxon potential (WSP) contains an elementary exponential form and depends upon three factors, namely depth of potential, diffuseness, and range [20–22].

In the present work, the fusion-fission dynamics of $^{12}C + ^{248}Cm$ and $^{16}O + ^{244}Pu$ reactions is analyzed using the symmetric-asymmetric Gaussian barrier distribution (SAGBD) model and dynamical cluster-decay model (DCM) in reference to the experimental measurements of Benerjee *et al.* [23] for these reactions. The SAGBD formalism contains a weighted Wong formula by the Gaussian function and multidimensional character of nucleus-nucleus potential, which incorporates the role of nuclear structure of the participants [24]. In this sense, the SAGBD approach [24] cumulatively considers all dominant channel coupling effects. Due to the multidimensional character of the SAGBD model, it compensates the effects of channel couplings appropriately and describes the fusion dynamics of $^{12}C + ^{248}Cm$ and $^{16}O + ^{244}Pu$ reactions around the Coulomb barrier in a reasonable way. In the SAGBD approach, the impact of channel couplings is analyzed in terms of the channel coupling parameter (λ) and percentage reduction of the effective fusion barrier (V_{CBRED}) with respect to the uncoupled Coulomb barrier (V_{CB}). The larger values of λ and V_{CBRED} imply a significant contribution from the nuclear structure of the fusing nuclei and hence reflects the need of a significant barrier modification in the fusion dynamics of the studied systems. The present work is focused on systems of different entrance channels forming the same compound nucleus ($^{260}No^*$). The enhanced fusion cross sections of $^{12}C + ^{248}Cm$ over $^{16}O + ^{244}Pu$ reactions imply that $^{12}C + ^{248}Cm$ has a larger entrance channel mass asymmetry over $^{16}O + ^{244}Pu$ and hence favors the fusion process. The λ and V_{CBRED} for the $^{12}C + ^{248}Cm$ ($^{16}O + ^{244}Pu$) reaction are, respectively, 2.53 (3.18) and 3.75% of V_{CB} (3.68% of V_{CB}) and thus point towards the presence of significant barrier modifications present in the SAGBD model.

To signify the impact of individual internal structure degrees of freedom associated with the collision partners, the coupled channel analysis for the $^{12}C + ^{248}Cm$ and $^{16}O + ^{244}Pu$ reactions has been done by using the coupled channel code CCFULL [25]. In both the reactions, the targets are statically deformed in their ground state and exhibit nonzero values of hexadecapole deformation ($\beta_4 = 0.039$ for ^{248}Cm and $\beta_4 = 0.062$ for ^{244}Pu). The projectile (^{12}C) is also statically deformed in its ground state while the heavier projectile (^{16}O) is doubly magic and spherical in shape in its ground state. Therefore, the rotational states of targets up to 10^+ spin states of the ground state rotational band of a target with $\beta_2 = 0.250$ for ^{248}Cm and $\beta_2 = 0.220$ for ^{244}Pu are included in the coupled channel description. In addition, the couplings to hexadecapole deformation ($\beta_4 = 0.039$ for ^{248}Cm and $\beta_4 = 0.062$ for ^{244}Pu) and a low lying quantum state of the projectiles are necessarily required in the coupled channel calculations in order to reproduce the experimental data of the considered reactions. For both reactions, the couplings to a low lying quantum state of the projectile are needed and hence found to contribute significantly. This clearly signifies the impacts of projectile degrees of freedom as well as the rotational states of the target isotopes along with hexadecapole deformation of the target for an adequate description of the observed subbarrier fusion enhancement for $^{12}C + ^{248}Cm$ and $^{16}O + ^{244}Pu$ reactions. The coupled channel analysis and the SAGBD analysis reflect almost a similar behavior of the studied reactions but via different mechanisms and thus both approaches reasonably describe the formation of the same compound nuclei via fusion channels.

After investigating the formation process of a compound nucleus (CN) exhibited via $^{12}C + ^{248}Cm$ and $^{16}O + ^{244}Pu$ reactions, the decay of compound nucleus $^{260}No^*$ formed in the above-mentioned reactions is analyzed by using the DCM [26–34] based upon the well-known quantum mechanical fragmentation theory (QMFT) [35–38]. Formerly, the fusion-fission studies were confined to reactions involving light mass projectiles such as protons, α, and stable heavy ions induced on stable targets such as gold, lead, and bismuth nuclei. Later, the discovery of radioactive nuclear beams to examine the fusion-fission decay patterns in heavy ion reactions became an exciting area of research. In such reactions, fusion may involve the complete amalgamation of the projectile and target nucleus, leading to a composite system which exhibits an excited state with specific excited energy (E^*), and also possesses a significant share of angular momentum. Further, the decay of different compound nuclei formed in a variety of heavy ion induced reactions at low energy range has become a compelling subject [39], since it helps to produce new isotopes that may not occur naturally. Moreover, such mechanisms also provide comprehensive knowledge of numerous nuclear properties and related structural and dynamical effects. The decay dynamics of the compound nucleus in the specified mass region ($A_{CN} \geqslant 200$) may also provide a lot of interesting opportunities [23], such as the exploration of the competing nature of different compound and noncompound nucleus (nCN) decay mechanisms such as fusion-evaporation, intermediate mass fragments, heavy mass fragments, fission fragments (symmetric/asymmetric), and noncompound nucleus decay processes (fast fission, quasifission), etc. Several experimental and theoretical efforts [26,40–49] have been made to examine the competing nature of CN and nCN processes. Various reaction conditions, such as incident energy, charge product, mass asymmetry, deformations, and orientations of the nuclei, play important roles in the emergence of CN and nCN mechanisms [26,40–49]. It has been observed [50,51] that in nCN processes, the fragments separate at a relatively shorter timescale as compared to the CN process. As a consequence, the barrier penetrability in nCN processes becomes a maximum, which results in a diminishing CN fission barrier. The main focus of the present work is to analyze $^{12}C + ^{248}Cm$ and $^{16}O + ^{244}Pu$ reactions,

which populate the same compound nucleus $^{260}No^*$. Here, the fusion-fission dynamics of the $^{260}No^*$ nucleus formed in the above-mentioned reactions at a wide range of center-of-mass energies range ($E_{c.m.} \approx 79$ to 109 MeV) is studied by including the quadrupole deformations (β_2) and optimum orientations (θ_i^{opt}) of the decay fragments. Furthermore, in reference to experimental data [23], the possibility of nCN contribution is also explored in the decay of the $^{260}No^*$ composite system. With an aim to have a comprehensive analysis of CN and nCN fission mechanisms, the role of center-of-mass energy ($E_{c.m.}$) and angular momentum (ℓ) is explored in terms of various parameters of DCM such as fragmentation potential, preformation probability, barrier modification, etc.

The paper is organized as follows. A brief description of the methodology used for the calculation is given in Sec. II. The results on fusion and corresponding decay dynamics are discussed in Sec. III, and the conclusions drawn are discussed in Sec. IV.

II. THEORETICAL FORMALISM

The theoretical formalism contains two subsections: (A) The SAGBD model: to analyze fusion data, the coupled channel analysis (wherever needed) is done by using the CCFULL code. (B) The DCM: to explain the decay process of the chosen systems.

A. SAGBD model

The total cross section on the basis of partial wave analysis for interacting nuclei is given by

$$\sigma_F = \frac{\pi}{k^2}\sum_{\ell=0}^{\infty}(2\ell+1)T_\ell^F. \tag{1}$$

Here, T_ℓ^F denotes the transmission probability through the fusion barrier for the ℓth wave and

$$k^2 = \frac{2\mu E_{c.m.}}{\hbar^2}, \tag{2}$$

wherein μ and $E_{c.m.}$ denote the fusing system reduced mass and energy incident in the center of mass frame. The transmission probability in one-dimensional BPM for the Coulomb barrier (V_{CB}) can be obtained by using the WKB method or solving the Schrödinger equation [52,53]. Hill and Wheeler suggested an expression for the probability of transmission (T_ℓ^{HW}) for the parabolic interaction barrier, and it is defined as [53]

$$T_\ell^{HW} = [1+\exp(\frac{2\pi}{\hbar\omega_\ell}(V_\ell - E_{c.m.}))]^{-1}, \tag{3}$$

where $\hbar\omega_\ell$ represents the barrier curvature associated with the effective barrier (V_ℓ) between fusing nuclei for the ℓth partial wave. In Eq. (1), by replacing T_ℓ^F with T_ℓ^{HW}, one can obtain the simple expression for the fusion cross section [4]

$$\sigma_F = \frac{\pi}{k^2}\sum_{\ell=0}^{\infty}(2\ell+1)T_\ell^{HW}. \tag{4}$$

Wong further simplified the Hill-Wheeler formula by using certain assumptions and obtained the following formula for calculations of fusion cross sections [54]:

$$\sigma^{Wong}(E_{c.m.}, V_{CB}) = \frac{\hbar\omega_B R_B^2}{2E_{c.m.}}\ln[1+\exp(\frac{2\pi}{\hbar\omega_B}(E_{c.m.}-V_{CB})], \tag{5}$$

where $\hbar\omega_B$, R_B, and V_{CB} are the barrier curvature, barrier position, and barrier height, respectively. The Wong formula has gained a lot of attention and was used most commonly because of its simplicity in the estimation of fusion cross sections. Nuclear potential between the fusing nuclei is assumed to be of Woods-Saxon type and is given by the following relation [4]:

$$V_N(r) = -\frac{V_0}{1+\exp\left(\frac{R-R_0}{a_0}\right)}, \tag{6}$$

where V_0 is the depth and a_0 is the diffuseness of the nuclear potential. The radius parameter R_0 is related to range parameter (r_0) via the following relation:

$$R_0 = r_0\left(A_P^{\frac{1}{3}} + A_T^{\frac{1}{3}}\right). \tag{7}$$

The range parameter (r_0) is related with the geometry of the fusing nuclei and its value depends upon the nature of the projectile and target isotopes. For spherical nuclei, the Coulomb potential is defined as

$$V_C(r) = \frac{Z_P Z_T e^2}{r}. \tag{8}$$

The total interaction potential for the s-partial wave ($\ell = 0$) is termed as Coulomb barrier and is defined as

$$V(r) = -\frac{V_0}{1+\exp(\frac{R-R_0}{a_0})} + \frac{Z_P Z_T e^2}{r}. \tag{9}$$

The height of the Coulomb barrier is defined by using the following relation:

$$V_{CB} = V(r)\big|_{r=R_B}, \tag{10}$$

where $V(r)$ denotes the total interaction potential between the collision partners. The peak position of the Coulomb barrier is obtained by using the following conditions:

$$\left.\frac{dV(r)}{dr}\right|_{r=R_B} = 0 \tag{11}$$

and

$$\left.\frac{d^2V(r)}{dr^2}\right|_{r=R_B} \leqslant 0. \tag{12}$$

The barrier curvature of the Coulomb barrier is evaluated by using the following conditions:

$$\hbar\omega_b = \left[\frac{-\hbar^2}{\mu}\frac{d^2V(r)}{dr^2}\right]^{\frac{1}{2}}\Bigg|_{r=R_B}. \tag{13}$$

The influences of channel coupling effects like rotational states, vibrational states of interacting nuclei, and/or transfer channels are not included in the Wong formula. In order to incorporate the influences of channel coupling effects, we have used the single weighted Gaussian function in the present

work. In other words, the fusion cross section is estimated by a weighting of the simple Wong formula by the single Gaussian function and such weighted cross sections include the impact of dominant channel couplings. In the SAGBD approach [24], the Wong formula as defined in Eq. (5) is a weighted Gaussian type of weight function and hence is described below. Following the Stelson's model [55] and the Swiek-Wilczynska and Wilczynska (SWW) model [56], the effective barrier distribution $D_f(V_{CB})$ obeys the following normalization condition:

$$\int D_f(V_{CB})dV_{CB} = 1. \tag{14}$$

The weighted Wong formula by a single Gaussian type function after taking into consideration the multidimensional character of the realistic interaction barrier is given by the following relation:

$$\sigma_F = \int_0^\infty D_f(V_{CB})\sigma^{\text{Wong}}(E_{\text{c.m.}}, V_{CB})dV_{CB}. \tag{15}$$

Here $\sigma^{\text{Wong}}(E_{\text{c.m.}}, V_{CB})$ denotes the Wong formula as given by Eq. (5). The single Gaussian function used to retrieve the practical barrier distribution form is given by the following equation:

$$D_f(V_{CB}) = \frac{1}{N}\exp\left[-\frac{V_{CB}-V_{B0}}{2\Delta^2}\right] \tag{16}$$

with $N = \Delta\sqrt{2\pi}$ and Δ in the equation is the standard deviation and corresponds to the half-width of the peak of the barrier distribution $D_f(V_{CB})$ at about 60% of the full width. In the present work, we extract a quantitative contribution of channel couplings which arises due to the nuclear structure of the participant. Such a contribution is described in terms of λ and V_{CBRED} with $V_{\text{eff}} \approx (0.95 \pm 0.03)V_{CB}$ and hence is defined as

$$\lambda = V_{CB} - (0.95 \pm 0.03)V_{CB}. \tag{17}$$

V_{CBRED} is defined as the percentage reduction of the effective fusion barrier with respect to the original Coulomb barrier and mathematically it is defined as

$$V_{\text{CBRED}} = \left[\frac{V_{CB}-V_{\text{eff}}}{V_{CB}}\right]100. \tag{18}$$

The coupled channel approach is a conventional method to handle the impacts of the channel coupling effects associated with the nuclear structure of participant nuclei on the fusion process. Within it, the following set of coupled channel equations is to be numerically solved [25]:

$$\left[\frac{-\hbar^2}{2\mu}\frac{d^2}{dr^2} + \frac{J(J+1)\hbar^2}{2\mu r^2} + V_N(r) + \frac{Z_P Z_T e^2}{r} + \varepsilon_n - E_{\text{c.m.}}\right]\Psi_n + \sum_m V_{nm}(r)\Psi_m = 0. \tag{19}$$

Here, $\overrightarrow{r}$ is the distance between the center of mass of the projectile and target nuclei. μ is the reduced mass of reacting nuclei. $E_{\text{c.m.}}$ and ε_n represent the incident energy in the center of mass frame and the excitation energy of nth channel, respectively. The $V_{nm}(r)$ are matrix elements of the coupling Hamiltonian, which in the collective model consists of the Coulomb and nuclear components. Ψ_n and Ψ_m are the wave functions in the nth and mth channels, respectively. V_N is the form of the nuclear potential used to analyze the experimental data. In code CCFULL [25], the coupled channel equations are solved numerically by adopting some simplifications like the rotating frame approximation and ingoing wave boundary conditions (IWBCs). In the coupled channel model, the impacts of intrinsic channels are incorporated through the static Woods-Saxon potential.

Since we are mainly interested in the inclusive process, where the intrinsic degrees of freedom emerge in any final state, therefore, by taking the sum over all the possible intrinsic states the total fusion cross section can be written as

$$\sigma_F(E_{\text{c.m.}}) = \sum_J \sigma_J(E_{\text{c.m.}}) = \frac{\pi}{k_0^2}\sum_J (2J+1)P_J(E_{\text{c.m.}}), \tag{20}$$

where k_0^2 is the wave vector in the entrance channel. $P_J(E)$, which includes the influences of the dominant intrinsic degrees of freedom associated with the colliding systems, is the total transmission coefficient corresponding to the total angular momentum J [25,57]. In coupled channel calculations, the vibrational couplings in the harmonic limit are taken into account and the rotational couplings are considered with a pure rotor assumption. In the rotational model, the nuclear coupling Hamiltonian can be generated by changing the target radius in the nuclear potential to a dynamical operator ($\hat{O}$),

$$R \to R_0 + \hat{O} \tag{21}$$

with $\hat{O}$ as the dynamical operator in rotational coupling and for a well deformed target nucleus it is defined as

$$R \to R_0 + \hat{O} = R_0 + \beta_2 R_T Y_{20} + \beta_4 R_T Y_{40} \tag{22}$$

with R_T parametrized as $r_{coup}A^{\frac{1}{3}}$, β_2 and β_4 are the quadrupole and hexadecapole deformation parameters of the deformed target nucleus, respectively. In general, the nuclear coupling matrix elements are evaluated as

$$V_N(r, \hat{O}) = -\frac{V_0}{1+\exp((r-R_0-\hat{O})/a)}. \tag{23}$$

We need matrix elements of this coupling Hamiltonian between the $|I0\rangle$ and $|I'0\rangle$ states of the ground rotational band of the target. These can be easily obtained using a matrix algebra wherein one first looks for the eigenvalues and eigenvectors of the operator $\hat{O}$. In the program CCFULL, using the diagonlization of the matrix for operator $\hat{O}$, the elements are given by

$$\hat{O}_{II'} = \sqrt{\frac{5(2I+1)(2I'+1))}{4\pi}}\beta_2 R_T \begin{pmatrix} I & 2 & I' \\ 0 & 0 & 0 \end{pmatrix}^2 + \sqrt{\frac{9(2I+1)(2I'+1))}{4\pi}}\beta_4 R_T \begin{pmatrix} I & 4 & I' \\ 0 & 0 & 0 \end{pmatrix}^2. \tag{24}$$

The total coupling matrix elements are obtained by taking the sum of $V_{nm}^{(N)}$ and $V_{nm}^{(C)}$ given as follows:

$$V_{nm}^{(N)} = \langle I0|V_N(r,\hat{O})|I'0\rangle - V_N^{(0)}(r)\delta_{n.m}$$
$$= \sum_a \langle I0|\alpha\rangle\langle\alpha|I'0\rangle V_N(r,\lambda_a) - V_N^{(0)}(r)\delta_{n.m}, \quad (25)$$

$$V_{nm}^{(C)} = \frac{3Z_PZ_T}{5}\frac{R_T^2}{r^3}\sqrt{\frac{5(2I+1)(2I'+1)}{4\pi}}$$
$$\times\left(\beta_2 + \frac{2}{7}\sqrt{\frac{5}{\pi}}\beta_2^2\right)\begin{pmatrix} I & 2 & I' \\ 0 & 0 & 0\end{pmatrix}^2$$
$$+ \frac{3Z_PZ_T}{9}\frac{R_T^4}{r^5}\sqrt{\frac{9(2I+1)(2I'+1)}{4\pi}}$$
$$\times\left(\beta_4 + \frac{9}{7}\beta_2^2\right)\begin{pmatrix} I & 4 & I' \\ 0 & 0 & 0\end{pmatrix}. \quad (26)$$

B. The dynamical cluster-decay model (DCM)

The fission mechanism of the hot and rotating $^{260}No^*$ nuclear system formed via $^{12}C + ^{248}Cm$ and $^{16}O + ^{244}Pu$ reactions at various center-of-mass energies $E_{c.m.}$ is analyzed using the DCM [26–38]. It is worked out in forms of

(i) collective coordinates of mass ($\eta_A = \frac{A_1-A_2}{A_1+A_2}$) and charge ($\eta_Z = \frac{Z_1-Z_2}{Z_1+Z_2}$) asymmetries where 1 and 2 stand, respectively, for heavy and light fragments;
(ii) relative separation R;
(iii) multipole deformations $\beta_{\lambda i}$ ($\lambda = 2, 3, 4$) and orientations θ_i of two nuclei or fragments.

The decay cross sections in DCM are calculated by using decoupled approximations to R and η motion and for the decoupled Hamiltonian, the Schrödinger wave equation reads as

$$\left[-\frac{\hbar^2}{2\sqrt{B_{\eta\eta}}}\frac{\partial}{\partial\eta}\frac{1}{\sqrt{B_{\eta\eta}}}\frac{\partial}{\partial\eta} + V_R(\eta,T)\right]\psi^\nu(\eta) = E_\eta^\nu\psi^\nu(\eta), \quad (27)$$

where $\nu = 0,1,2...$ refers to ground, first, and second state solutions, respectively, and $B_{\eta\eta}$ is the smooth hydrodynamical mass parameter [58].

The fragmentation potential $[V_R(\eta, T)]$ in Eq. (27) is calculated by a summation of (i) V_{LDM} (T-dependent liquid drop energy of Davidson [59]) with its constants at $T = 0$ MeV refitted [38] to give the experimental binding energies [60,61]; (ii) δU, the empirical shell corrections of Myers and Swiatecki [62]; and (iii) V_C, V_P, and V_ℓ are, respectively, the T-dependent Coulomb, nuclear proximity, and angular momentum dependent potentials for deformed and oriented nuclei. The expression for $V_R(\eta, T)$ is given as

$$V_R(\eta,T) = \sum_{i=1}^{2}[V_{LDM}(A_i,Z_i,T)] + \sum_{i=1}^{2}[\delta U_i]\exp\left(-T^2/T_0^2\right)$$
$$+ V_C(R,Z_i,\beta_{\lambda i},\theta_i,T) + V_P(R,A_i,\beta_{\lambda i},\theta_i,T)$$
$$+ V_\ell(R,A_i,\beta_{\lambda i},\theta_i,T). \quad (28)$$

Here, T_0 is considered as $T_0 = 1.5$ MeV and it is the temperature at which shell effects are considered to vanish exponentially for higher excitation energies.

Further, the formation yield of decaying fragments is worked out by calculating the preformation factor (P_0) (containing the structure information of the compound nuclear system) as a solution of Eq. (27) and the equation for P_0 is given as

$$P_0 = |\ \psi(\eta(A_i))\ |^2\ \sqrt{B_{\eta\eta}}\frac{2}{A_{CN}}. \quad (29)$$

The preformation factor (P_0) shown in Eq. (29) refers to η motion. Further, A_i ($i = 1, 2$) represents the mass of fragments of outgoing channel and A_{CN} is the mass of the compound nucleus.

Next, in the tunneling process, the barrier penetrability "P" of clusters or fragments refers to R motion and is calculated by using the Wenzel-Kramers-Brillouin (WKB) integral as

$$P = \exp\left[-\frac{2}{\hbar}\int_{R_a}^{R_b}\{2\mu[V(R) - Q_{\rm eff}]\}^{1/2}dR\right]. \quad (30)$$

$V(R)$ in Eq. (30) represents the scattering potential and is defined as the sum of the Coulomb potential, proximity potential, and angular momentum dependent potential $[V(R) = V_C(R,Z_i,\beta_{\lambda i},\theta_i,T) + V_P(R,A_i,\beta_{\lambda i},\theta_i,T) + V_\ell(R,A_i,\beta_{\lambda i},\theta_i,T)]$. Further $Q_{\rm eff} = B(T) - [B_1(T=0) + B_2(T=0)]$ is the effective Q value, for the decay of the hot compound nucleus at temperature T into two binary fragments observed in the ground state ($T = 0$) with their binding energies B_i ($i = 1, 2$).

Furthermore, R_a in Eq. (30) is the first turning point of the barrier penetration and is defined as

$$R_a = R_1(\alpha_1,T) + R_2(\alpha_2,T) + \Delta R(T)$$
$$= R_t(\alpha,T) + \Delta R(T) \quad (31)$$

with radius vectors (i = 1,2)

$$R_i(\alpha_i,T) = R_{0i}(T)\left[1 + \sum_\lambda \beta_{\lambda i}Y_\lambda^{(0)}(\alpha_i)\right] \quad (32)$$

and T-dependent nuclear radii $R_{0i}(T)$ of the equivalent spherical nuclei [63],

$$R_{0i}(T) = \left[1.28A_i^{1/3} - 0.76 + 0.8A_i^{-1/3}\right](1 + 0.0007T^2). \quad (33)$$

In the definition of R_a above, ΔR is the neck length parameter, which represents the relative separation distance between two fragments. It decides the first turning point of barrier penetration, referring to the actually used barrier height, and also allows us to define the barrier modification, $\Delta V_B = V(R_a) - V_B$, which relates $V(R_a)$ and the top of the barrier V_B. Further, the nuclear temperature (T) used above is related to the compound nucleus excitation energy as $E_{CN}^* = (A_{CN}/9)T^2 - T$.

Finally, after getting P and P_0, the expression of the decay cross section is given by

$$\sigma = \sum_{\ell=\ell_{\min}}^{\ell_{\max}}\sigma_\ell = \frac{\pi}{k^2}\sum_{\ell=\ell_{\min}}^{\ell_{\max}}(2\ell+1)P_0P; \quad k = \sqrt{\frac{2\mu E_{\rm c.m.}}{\hbar^2}}, \quad (34)$$

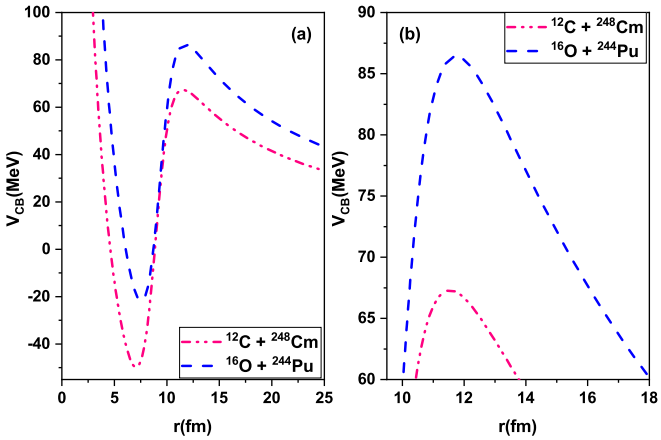

FIG. 1. (a) The variation of the Coulomb barrier (V_{CB}) as a function of radial separation (r) between projectile and target for ^{12}C + ^{248}Cm and ^{16}O + ^{244}Pu reactions and (b) an amplified version of (a) near barrier positions and calculations is obtained by using the SAGBD model.

where $\mu = [A_1A_2/(A_1 + A_2)]m$ is the reduced mass, and $\ell_{\min}$ (where the decay cross section starts contributing) and $\ell_{\max}$ are the minimum and maximum angular momentum, respectively. For CN mechanisms, the maximum angular momentum is ℓ_{bf}^{CN} [64], above which compound nucleus formation is hindered (or fission barrier diminishes), and for nCN, $\ell_{\max}$ is the upper limit of the partial wave above the ℓ_{bf}^{CN} value up to which the nCN peripheral collisions participate in the fission dynamics.

III. RESULTS AND DISCUSSION

A. Fusion analysis of ^{12}C + ^{248}Cm and ^{16}O + ^{244}Pu reactions

A comparison between Coulomb barriers of the chosen reactions is shown in Fig. 1. From this figure, it has been observed that the Coulomb barrier height varies for various systems. In other words, there is a variation in the radial dependency of interaction barriers at the peak that induces the different barrier characteristics for the chosen reactions. As a consequence, the sub-barrier enhancement in the magnitude of the fusion excitation function depends on the combination of colliding partners. We took the Woods-Saxon parametrization of the nucleus-nucleus potential for the fusion analysis. The sub-barrier fusion data are highly dependent on intrinsic degrees of freedom linked with the structure of interacting nuclei, while above barrier fusion data are resistant to the effects of channel coupling. Hence, the above barrier fusion data may be replicated by one-dimensional BPM. The potential depth (V_0), the diffuseness (a_0), and range parameter (r_0) for the studied systems are listed in Table I and are used to retrieve the behavior of the fusion excitation functions. By taking the values of the potential parameter as given in Table I, the barrier characteristics such as Coulomb barrier (V_{CB}), peak position (R_B), and the barrier curvature ($\hbar\omega_B$) are obtained by employing the conditions as defined by Eqs. (10) to (13) and are given in Table II. The radial dependency of the regular WSP, Coulomb potential, and the Coulomb barrier for various systems is depicted in Fig. 2. The barrier formed by combining the attractive nuclear potential (V_N) and repulsive Coulomb potential (V_C) is termed the Coulomb barrier (V_{CB}). The dashed line in every panel indicates the radial dependency of the Coulomb potential, while the dash dot-dot line in every panel indicates the radial dependence of the nuclear potential.

TABLE I. The parameters of the Woods-Saxon potential such as depth (V_0), diffuseness (a_0), and range (r_0), which have been used to analyze the experimental data for different heavy ion fusing systems.

S. No.	Colliding systems	V_0 (MeV)	a_0 (fm)	r_0 (fm)
1	^{12}C + ^{248}Cm	180	0.72	1.04
2	^{16}O + ^{244}Pu	180	0.72	1.06

If channel coupling effects are absent then the main peak of the barrier distribution appears around the Coulomb barrier. However, owing to the nuclear structure effects, the height and shape of the main peak of the barrier distribution varies towards the left or right side of the Coulomb barrier and these results are expressed in the SAGBD model in terms of the channel coupling parameter (λ). Thus, λ intrinsically refers to different kinds of nuclear structure degrees of freedom that are responsible for enhancing the sub-barrier fusion data. The $V_{\rm CBRED}$ parameter reflects the percentage reduction or deviation of the effective fusion barrier between interacting nuclei due to the consideration of different nuclear structure effects associated with interacting nuclei with respect to the uncoupled Coulomb barrier (V_{CB}). These parameters ($V_{\rm eff}$, $V_{\rm CBRED}$, and λ) have been extracted from the SAGBD analysis and are listed in Table III.

Figures 3(a) and 3(b) represent the total fusion excitation functions for ^{12}C + ^{248}Cm and ^{16}O + ^{244}Pu systems calculated by using the Wong formula and SAGBD model. The solid line represents the estimations taken by using the SAGBD model for every figure, while the dash dot dot line corresponds to Wong estimations and the experimental data is denoted by symbols depicted in the figure. The estimated fusion excitation functions are significantly underpredicted in comparison with the experimental findings because the simple Wong formula does not include the impacts of the channel couplings that result due to the nuclear geometry of the interacting nuclei. The deviations between theoretical results and experimental data are a maximum at below barrier energies and these deviations do not appear in the above barrier regions. This indicates that above barrier fusion data have negligible dependence on the intrinsic structure of participating nuclei.

TABLE II. The values of Coulomb barrier (V_{CB}), barrier position (R_B), and barrier curvature ($\hbar\omega_B$) for different heavy ion fusing systems.

S. No.	Colliding systems	V_{CB} (MeV)	R_B (fm)	$\hbar\omega_B$ (MeV)
1	^{12}C + ^{248}Cm	67.29	11.54	4.43
2	^{16}O + ^{244}Pu	86.40	11.74	5.07

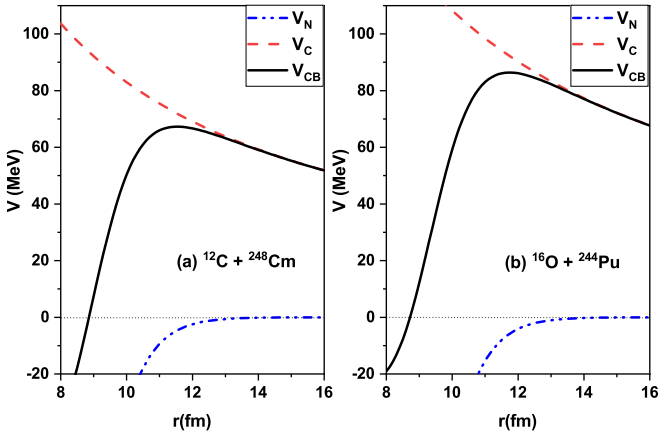

FIG. 2. The variations of the Coulomb (V_C) and nuclear (V_N) potentials along with the Coulomb barrier (V_{CB}) as a function of radial separation between projectile and target for (a) $^{12}C+^{248}Cm$ and (b) $^{16}O+^{244}Pu$ reactions calculations are obtained by using the SAGBD model.

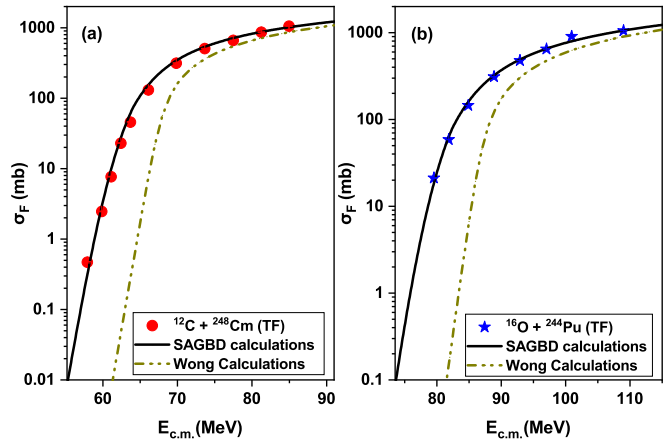

FIG. 3. The total fusion cross section for (a) $^{12}C+^{248}Cm$ and (b) $^{16}O+^{244}Pu$ reactions as a function of $E_{c.m.}$ obtained by using the Wong formula and SAGBD model. These results are compared with the experimental data taken from Ref. [23].

However, the channel coupling effects caused by the nuclear composition of the fusing partners are crucially important in the sub-barrier realm and, without recognizing them, the total fusion data cannot be replicated at near and below the Coulomb barrier.

Benerjee *et al.* [23] experimentally measured the excitation function for the formation of the $^{260}No^*$ compound nucleus in the energy range $E_{c.m.} = 57.91$ to 84.96 MeV (for the $^{12}C+^{248}Cm$ system) and $E_{c.m.} = 79.54$ to 109.01 MeV (for the $^{16}O+^{244}Pu$ system). The authors suggested that the mass-asymmetry structure of the $^{12}C+^{248}Cm$ system is found to be larger than that of the $^{16}O+^{244}Pu$ system. Owing to the presence of multidimensional character, the SAGBD model predictions automatically sustain the influential channel-coupling effects in the sub-barrier fusion mechanism of the chosen reactions. The multidimensional nature of the nucleus-nucleus potential that emerged due to the Gaussian type of weight function, hence reflects inherently the influence of nuclear structure in the SAGBD estimations. This lowers the fusion barrier between the collision partners and, as a result, the SAGBD model predicts larger fusion cross sections in the sub-barrier domain. In this manner, the model results shift towards experimental data in below-barrier energy regions, and thus explain the reported fusion enhancements with respect to the predictions of one-dimensional BPM. Thus, the SAGBD predictions appropriately describe the fusion mechanism of $^{12}C+^{248}Cm$ and $^{16}O+^{244}Pu$ systems qualitatively. On the other hand, the impacts of channel couplings are described in terms of channel coupling parameters (λ) and the percentage reduction of the effective barrier height (V_{CBRED}) with respect to original barrier and results are listed in Table III. The value of λ for $^{12}C+^{248}Cm$ and $^{16}O+^{244}Pu$ systems is found to be 2.53 and 3.18, respectively. The larger value of λ implies that the channel couplings are significant at sub-barrier energies and hence greater barrier modifications are needed for an adequate fusion description of the dynamics of studied reactions. Besides the presence of a nucleon transfer channel in the $^{16}O+^{244}Pu$ system, the sub-barrier fusion enhancement of this system is lower than that of the $^{12}C+^{248}Cm$ reaction. This fact can be correlated with the larger entrance channel mass asymmetry for the $^{12}C+^{248}Cm$ reaction. The value of V_{CBRED} for the $^{12}C+^{248}Cm$ and $^{16}O+^{244}Pu$ systems is found to be 3.75% and 3.68% of V_{CB}, respectively.

TABLE III. The values of channel coupling parameter λ and V_{CBRED} for the chosen reactions under study.

S. No.	Colliding systems	V_{CB} (MeV)	V_{eff} (MeV)	λ (fm)	V_{CBRED}
1	$^{12}C+^{248}Cm$	67.29	64.76	2.53	3.75% of V_{CB}
2	$^{16}O+^{244}Pu$	86.40	83.22	3.18	3.68% of V_{CB}

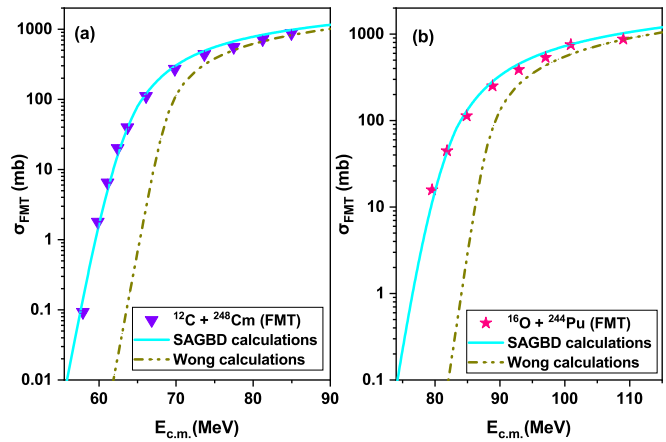

FIG. 4. The full momentum transfer (FMT) or [complete fusion (CF) cross section] of (a) $^{12}C+^{248}Cm$ and (b) $^{16}O+^{244}Pu$ reactions as a function of $E_{c.m.}$ obtained by using the Wong formula and SAGBD model. These results are compared with the experimental data taken from Ref. [23].

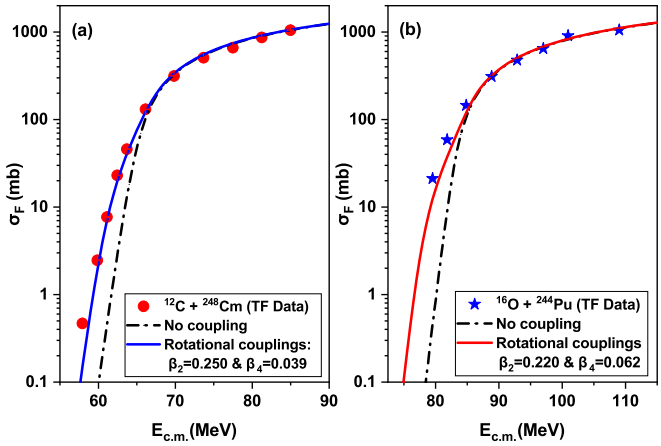

FIG. 5. The total fusion cross section for (a) $^{12}C + ^{248}Cm$ and (b) $^{16}O + ^{244}Pu$ reactions as a function of $E_{c.m.}$ obtained by using coupled channel code CCFULL. These results are compared with the experimental data taken from Ref. [23].

Figures 4(a) and 4(b) represent the complete fusion cross sections for the $^{12}C + ^{248}Cm$ and $^{16}O + ^{244}Pu$ systems obtained by using the Wong formula and SAGBD model. As already mentioned the simple Wong formula does not include the influences of the nuclear structure of reaction partners, therefore, the predictions of complete fusion cross sections remain significantly lower than the experimental data. On the other hand, the SAGBD model obtains the required order of the CF cross sections due to the multidimensional nature of the nucleus-nucleus interaction potential. The calculated results for chosen reactions are compared with the CF data in Fig. 4.

In order to identify the effects of the internal structure degrees of freedom of the collision partners, the coupled channel calculations are performed by using the coupled channel code CCFULL and the results of calculations are shown in Fig. 5. The parameters of the standard Woods-Saxon potential, such as potential depth, diffuseness, and range parameter, which are used in the coupled channel code CCFULL for performing the coupled channel calculations, are listed in Table IV. These potential parameters are chosen in such a way that the above barrier fusion data can be reasonably revolved by using no coupling calculations. The ground state deformation parameters and corresponding excitation energies of the target and the low lying quantum states such as 2^+ and 3^- vibrational states of the projectiles are taken from Refs. [9,65–67] and

TABLE IV. The parameters of the Woods-Saxon potential such as depth (V_0), diffuseness (a_0), and range (r_0), which have been used in the coupled channel code CCFULL for the coupled channel calculations of the present fusing systems.

S. No.	Colliding systems	V_0 (MeV)	a_0 (fm)	r_0 (fm)
1	$^{12}C + ^{248}Cm$	150	0.66	1.130
2	$^{16}O + ^{244}Pu$	150	0.66	1.150

TABLE V. The deformation parameters and corresponding excitation energies of low lying quantum states which are used in the coupled channel calculations of the present reactions which are taken from Refs. [9,65–67].

Nucleus	β_2	E_2 (MeV)	β_3	E_3 (MeV)
^{12}C	0.592	4.440	1.550	9.640
^{16}O	0.350	6.920	0.710	6.130
^{248}Cm	0.250	0.0434	–	–
^{244}Pu	0.220	0.0442	–	–

are listed in Table V. For both cases, the coupled channel calculations are obtained by incorporating the rotational states up to 10^+ spin states of the ground state rotational band of target isotopes. Additionally, the couplings to higher order deformation, such as β_4 for target and 2^+ quantum states of the projectile, which are found to play a very important role in the sub-barrier fusion enhancement of the given reactions, are also incorporated for addressing the experimental data of the studied systems.

For the $^{12}C + ^{248}Cm$ reaction, the no coupling calculations, in which the colliding systems are taken as point-like particles and their internal structure are ignored, are substantially smaller than those of the experimentally observed data particularly in below barrier energy regions. As far as the projectile is concerned, it is statically deformed in its ground state, therefore, the quadrupole deformation of the projectile is expected to affect the fusion dynamics of the studied system. The deformation parameter for the quadrupole state of the target is much larger than that of its octupole deformation. Additionally, the excitation energy corresponding to the 2^+ vibrational state lies much lower than that of its 3^- vibrational state as given in Table V, therefore, the couplings of the relative separation coordinate with a 2^+ vibrational state are expected to influence the fusion yields at sub-barrier energies. The couplings to the rotational states up to 10^+ spin states of the ground state rotational band of target isotopes enhance the magnitude of the fusion cross sections in below barrier energy regions with respect to the outcomes of the one-dimensional BPM as evident from Fig. 5(a). Additionally, the couplings to higher order deformation such as β_4 for the target and 2^+ quantum states of the projectile, which are found to play a very important role in the sub-barrier fusion enhancement of the given reactions, are also incorporated for addressing the experimental data of the studied systems. The so-obtained calculations are unable to address the experimental data in sub-barrier energy regions but these calculations reasonably recover the experimental data at above barrier energies. To improve the theoretical outcomes, the coupling to $\beta_4 = 0.039$ is included in the coupled channel description. Such calculations further converge the calculations towards the data in sub-barrier energy regions but fail to reproduce the experimental data. This demands couplings to more intrinsic degrees of freedom of the collision partner in the coupled channel calculations. Therefore, the couplings to one phonon 2^+ vibrational state of the projectile as well as rotational states up to 10^+ spin states of the ground state rotational band of

target isotopes along with $\beta_4 = 0.039$ of the target are done in the coupled channel code CCFULL. The so-obtained coupled channel calculations adequately describe the sub-barrier fusion dynamics of the present reaction in the whole range of incident energy as depicted in Fig. 5(a). In this sense, the couplings to dominant vibrational excitations of the participants appropriately describe the observed fusion dynamics of the chosen system.

In the case of the $^{16}O + ^{244}Pu$ reaction, the no coupling estimations remain substantially underestimated with reference to the experimental data in the below barrier energy range. This is due to the fact that no coupling outcomes, except for the relative motion between the participants, entertain the additional intrinsic degrees of freedom associated with the collision partners. To address the experimental data, the couplings to internal structure degrees of freedom of the projectile and target must be incorporated in the coupled channel analysis. As the target isotope is well deformed in its ground state, is reasonable to consider the rotational states of the target rather than its vibrational states. The considerations of the rotational states up to 10^+ spin states of the ground state rotational band of the target substantially increase the fusion probability as well as the fusion yields particularly in sub-barrier energy regions. The inclusion of the rotational states of the target along with $\beta_4 = 0.062$ of the target is not sufficient to account for the observed sub-barrier fusion dynamics of a given reaction. The couplings to additional intrinsic degrees of freedom associated with the projectile are needed to reproduce the sub-barrier fusion enhancement of the chosen reaction. Although, the projectile is a doubly magic nucleus and the vibrational states of this nucleus lie at much higher excitation energies, the one-phonon 3^- vibrational state of the projectile is included in the coupled channel description. Thus, by entertaining the rotational states up to 10^+ spin states of the ground state rotational band of the target along with $\beta_4 = 0.062$ of the target and the one-phonon 3^- vibrational state of the projectile, the coupled channel calculations properly describe the sub-barrier fusion anomaly of the present reaction as evident from Fig. 5(b). Besides the projectile vibrational states lying at much higher excitation energies, the projectile contributes to the fusion process significantly and hence unambiguously identifies the participation of the projectile degrees of freedom in the fusion dynamics of the $^{16}O + ^{244}Pu$ reaction.

In Fig. 6, the fusion excitation functions for the $^{12}C + ^{248}Cm$ and $^{16}O + ^{244}Pu$ systems are plotted as a function of $\frac{E_{c.m.}}{V_{CB}}$. Both reactions have separate entrance channels, but they form the same compound nucleus, i.e., ($^{260}No^*$). In literature [19,24], it has been emphasized that greater entrance channel mass asymmetry ($\eta = |\frac{A_P - A_T}{A_P + A_T}|$) supports the mechanism of fusion reactions resulting in the enhancement of the fusion cross sections at the sub-barrier realm. Thus, η can influence the fusion mechanism of the chosen reactions and its magnitude is 0.907 for the $^{12}C + ^{248}Cm$ reaction and 0.877 for the $^{16}O + ^{244}Pu$ reaction. The larger value of η for the $^{12}C + ^{248}Cm$ system as compared to the $^{16}O + ^{244}Pu$ system causes some extra fusion enhancement in the sub-barrier domain for the earlier case.

In Fig. 7, the comparison of theoretical predictions based upon the SAGBD model and coupled channel approach has

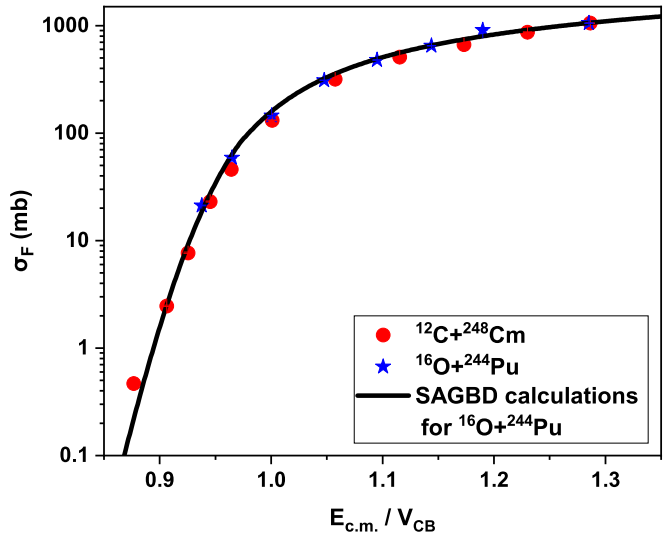

FIG. 6. Fusion cross sections data for (a) $^{12}C + ^{248}Cm$ and (b) $^{16}O + ^{244}Pu$ reactions are compared in reduced scale $E_{c.m.}/V_{CB}$. The experimental data of the chosen reactions are taken from Ref. [23].

been made and, from this figure, it is unambiguously clear that the SAGBD model predictions and coupled channel calculations reflect an almost similar behavior of the studied reactions in the close vicinity of the Coulomb barrier. The coupled channel calculations performed by incorporating the appropriate number of intrinsic channels associated with the collision partners fairly reproduce the experimental data of $^{12}C + ^{248}Cm$ and $^{16}O + ^{244}Pu$ systems in near and sub-barrier energy regions. In a similar sense, the Gaussian type of weight function used in the SAGBD model properly includes the cumulative influences of the all the dominant intrinsic channels that are responsible for the observed sub-barrier fusion enhancement of the chosen reaction. The Gaussian type

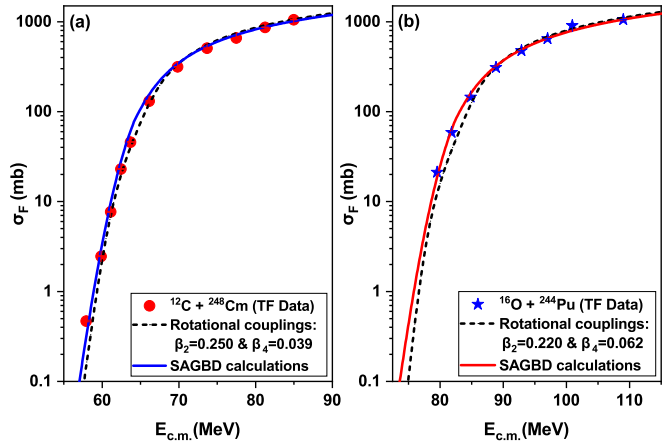

FIG. 7. The total fusion cross sections obtained by using the coupled channel approach and SAGBD model are compared for (a) $^{12}C + ^{248}Cm$ and (b) $^{16}O + ^{244}Pu$ reactions as a function of $E_{c.m.}$. The calculated results are also compared with the experimental data taken from Ref. [23].

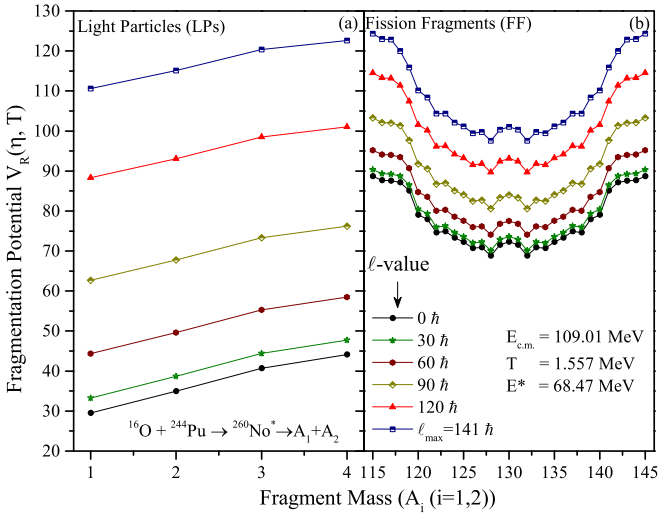

FIG. 8. Variation of fragmentation potential of (a) light particles and (b) fission fragments as a function of fragment mass in the decay of hot and rotating ^{260}No* composite system at $E_{\text{c.m.}} = 109.01$ MeV for different ℓ- ranging $0 \leqslant \ell \leqslant \ell_{\max}$.

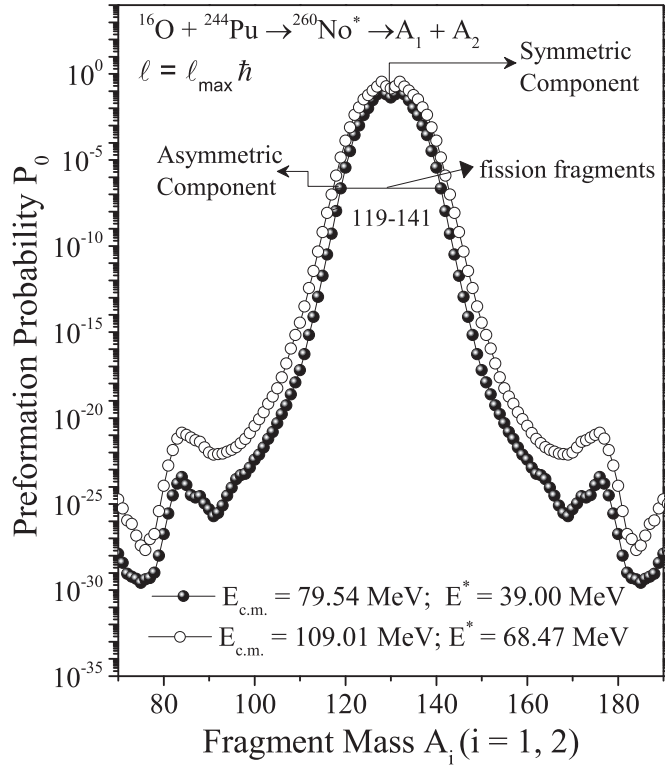

FIG. 9. Variation of preformation probability (highlighting the fission region) as a function of fragment mass at two extreme energies.

of weight function taken in the present work seems to be reasonable for explaining the behaviors of the heavy ion fusion dynamics.

After studying the fusion process of ^{12}C + ^{248}Cm and ^{16}O + ^{244}Pu reactions, the subsequent decay analysis of compound nucleus ^{260}No* is analyzed in the next section.

B. Fission analysis of the ^{260}No* nucleus

1. Induced fission

This section deals with the decay study of ^{260}No* at the center-of-mass energies spread $E_{\text{c.m.}} \approx 79$ to 109 MeV by including the quadrupole deformations (β_2) and optimum orientations (θ_i^{opt}) of the decay fragments. According to the experimental observation, the nCN fission component competes with the CN fission process for the chosen CN. Consequently, the possibility of nCN contribution is also explored in the decay of the ^{260}No* compound nucleus. With an aim to have comprehensive analysis of the CN and nCN fission mechanism, the role of the center-of-mass energy ($E_{\text{c.m.}}$) and angular momentum (ℓ) is explored in terms of various observables of DCM such as the fragmentation potential, preformation probability, and barrier modification.

First to understand the decay of the ^{260}No* composite system formed in the ^{16}O + ^{244}Pu reaction, the fragmentation behavior of light particles and fission fragments is studied. Figure 8 depicts the fragmentation potential $V_R(\eta, T)$ for light particles and fission fragments (FF) in the decay of the ^{260}No* nucleus at maximum given center of mass energy, $E_{\text{c.m.}} = 109.01$ MeV at different values of angular momentum ranging from $0 \leqslant \ell \leqslant \ell_{\max}$. The calculated T-dependent collective potential energy $V_R(\eta, T)$ gives the relative contribution of possible decay fragments. It is noticed from Fig. 8 that lower ℓ states are energetically more favorable for light particles (LPs) and higher ones for the FF. This implies that at lower ℓ values the probability of LPs to participate in the decay process is comparatively more than that of the fission fragments. Because at lower ℓ values the fragmentation potential ($[V_R(\eta, T)]$ of LPs is less than that of fission fragments as shown in the figure. A lesser fragmentation potential signifies more of a possibility of fragments to participate in the decay channel. However, if we compare $V_R(\eta, T)$ of LPs and fission fragments at higher ℓ values, the value of $V_R(\eta, T)$ is lesser for fission in comparison to that of LPs. Therefore, at higher angular momentum, the fission region acquires a lower fragmentation potential (equivalently, the higher the preformation probability P_0) in comparison to light particles. This confirms that the fission component dominates at higher ℓ value. Furthermore, it is important to mention here that the value of $V_R(\eta, T)$ increases with an increase in the ℓ value for both decay modes. However, the structure of the fragmentation potential for both light particles and fission fragments is observed to remain similar at all ℓ values. The variation of the potential energy surfaces reveals that ^{260}No* shows nearly symmetric mass distribution, which is in line with the experimental observation [23]. The same observation is drawn at other energies (not shown here to avoid repetition). It is relevant to mention that, in the framework of DCM, the preformation factor P_0 is the solution of the stationary Schrödinger equation in the η coordinate, where the fragmentation potential goes as input [see Eq. (27)].

After studying the variation of the fragmentation potential, we analyze the decay dynamics of the ^{16}O + ^{244}Pu reaction through the preformation probability P_0 (see Fig. 9), plotted as

TABLE VI. The DCM-calculated fission cross sections for the $^{260}No^*$ nucleus at center-of-mass energies ranging from $E_{c.m.}$ = 79.54 to 109.01 MeV. Also tabulated are the relevant fitted neck-length parameters ΔR, temperatures T, and excitation energies (E^*).

S. No.	$E_{c.m.}$ (MeV)	E^* (MeV)	ℓ_{max} ($\hbar$)	ΔR (fm)	σ_{FMT}^{DCM} (mb)	σ_{FMT}^{exp} (mb)
1	79.54	39.00	134	0.974	15.50	15.8 ± 0.2
2	81.84	41.30	134	1.001	43.80	44.7 ± 0.5
3	84.87	44.33	135	1.026	113.74	113.2 ± 0.9
4	88.86	48.32	136	1.057	251.38	250.7 ± 1.7
5	92.89	52.35	137	1.077	391.69	388.6 ± 2.4
6	97.03	56.49	138	1.089	543.60	538.6 ± 2.4
7	100.93	60.39	139	1.108	752.00	754.0 ± 2.2
8	109.01	68.47	141	1.200	876.00	874.0 ± 5

a function of heavy mass fragments at ℓ_{max}, as the fission contribution becomes prominent at higher ℓ values. Comparing the preformation profile at extreme energies, it is observed that the magnitude of P_0 changes very minutely. Also, the mass distribution for fission fragments is almost identical and symmetric in nature, independent of $E_{c.m.}$. Furthermore, the fission cross sections for $^{260}No^*$ at all given energies are addressed by optimizing the neck length parameter (ΔR), the only parameter of the DCM, and are tabulated in Table VI along with other essential quantities. It is clearly observed from the table that the DCM calculated cross sections are in good agreement with the experimental data [23]. The neck length parameter may be used to estimate the barrier modification (ΔV_B) for the decay of the compound nucleus. Thus, to extend the fission analysis of the $^{260}No^*$ compound system, ΔV_B, which is an in-built barrier lowering property of the DCM, is scrutinized as a function of center of mass energy for both symmetric and asymmetric fission components in Fig. 8.

Figure 10 depicts the variation of $|\Delta V_B|$ as a function of center of mass energy for the fission decay of the $^{260}No^*$ compound system for both symmetric and asymmetric fission components at extreme ℓ values. It is observed from the

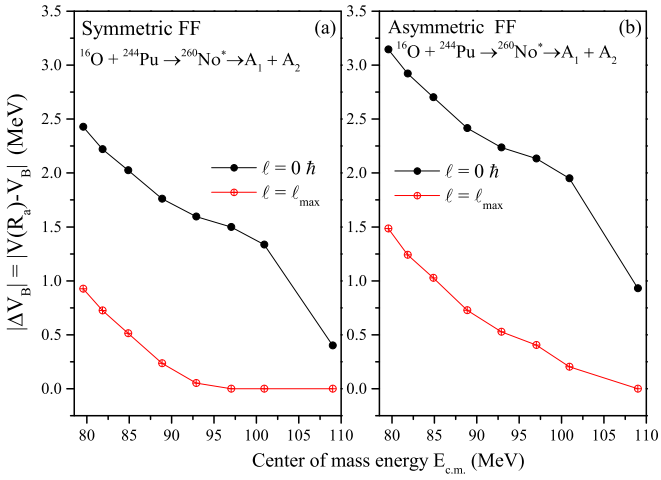

FIG. 10. Variation of $|\Delta V_B| = |V(R_a) - V_B|$ as a function of center of mass energy ($E_{c.m.}$) for symmetric and asymmetric fission fragment at extreme ℓ values.

figure that the magnitude $|\Delta V_B|$ is lower for the symmetric component. This signifies that the asymmetric fission component demands higher barrier modification to participate in the fission decay of the $^{260}No^*$ compound system. Further, $|\Delta V_B|$ is highest at the lowest energy and at lower ℓ value. This implies that $|\Delta V_B|$ decreases with an increasing value of the angular momentum and $E_{c.m.}$. As a consequence, a larger barrier modification is required at lower energies and lower ℓ values. Further, one may also observe that at the higher three energies for maximum ℓ state, the magnitude $|\Delta V_B|$ almost approaches zero. This corresponds to the disappearance of the fission barrier at a large value of angular momentum due to higher rotational energy, which inhibits the formation of an equilibrated compound nucleus at higher ℓ values [64]. This signifies that a hot and rotating composite system undergoes the nCN process, and may lead to the formation of nCN fission fragments similar to those in the fusion-fission (ff) process at higher ℓ states [64]. This claim is in agreement with the referred experimental data [23].

In view of this, an attempt is made to estimate the nCN fission cross sections at the higher three energies ($E_{c.m.}$ = 97.03, 100.93, 109.01 MeV). Now, for ℓ values, where the fission barrier disappears, the barrier penetrability is maximum [68]. The nCN cross sections (σ_{nCN}) are estimated by summing the fission contribution of fragments, at those ℓ values where the fission barrier starts vanishing or the barrier penetrability [see Eq. (30)] becomes one [64]. The σ_{nCN} values calculated using the DCM are depicted in Fig. 11. This figure reveals the variation of nCN fission cross sections as a function of the fragment mass at $E_{c.m.}$ = 97.03, 100.93, 109.01 MeV. It is observed from the figure that with an increase in energy, nCN contribution increases with a maximum at $E_{c.m.}$ = 109.01 MeV. Furthermore, Fig. 11 clearly shows that unlike CN fission, the mass distribution of nCN fission fragments is purely asymmetric in nature, which is in line with the experimental estimate [23].

Next, to analyze the entrance channel effects on CN fission, the fission study of another incoming channel $^{12}C + ^{248}Cm$ forming a $^{260}No^*$ compound nucleus is also demonstrated at common $E_{c.m.}$ in order to make a comparison between the mass distribution profile of the $^{260}No^*$ compound system while considering both incoming channels ($^{12}C + ^{248}Cm$ and $^{16}O + ^{244}Pu$). It is important to note that the calculations for the latter incoming channel are done only at the two extreme energies, i.e., $E_{c.m}$ = 81.24 and 84.96 MeV. The calculated fission cross sections match the experimental data nicely and the corresponding neck length parameter for both the energies is nearly ΔR = 1.0 fm. Figure 12 represents the preformation distribution of $^{260}No^*$ at center of mass energy, i.e., 81.24 MeV for a maximum value of angular momentum while using the hot oriented deformed approach. It is observed that the structural profile remains almost the same for both incoming channels, although a minute difference in their magnitudes is visible. A nearly symmetric fission peak is exhibited for both cases and the fragments contributing towards fission cross sections are identical. The fragment having the maximum probability to be preformed is ^{128}Sn (with complementary fragment ^{132}Te). Both emitting fragments are near the magic closure Z = 50 and N = 82.

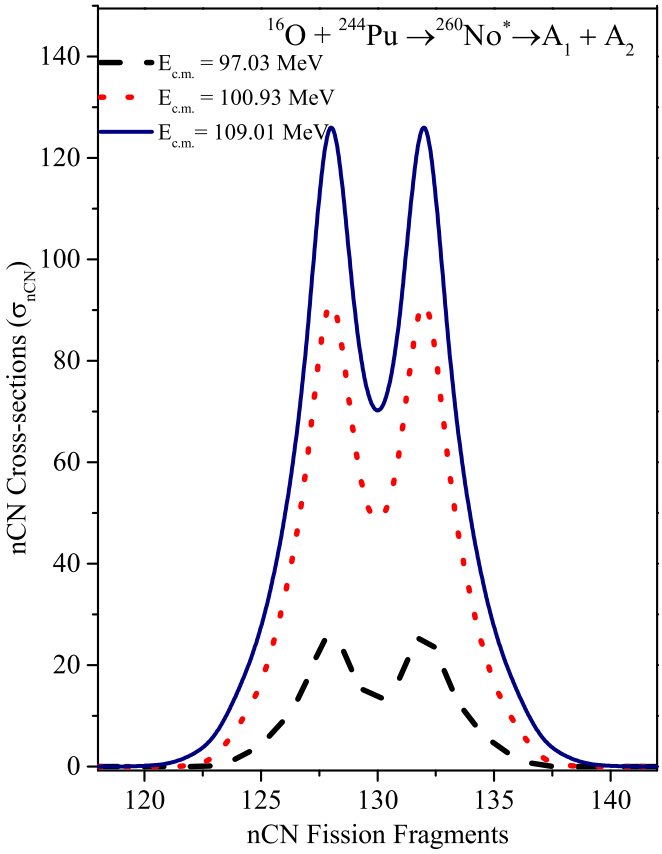

FIG. 11. Variation of nCN cross sections for fission fragments contributing to nCN decay.

2. *Spontaneous fission*

Now, it is a well known fact that nobelium, being a highly fissile nucleus, exhibits spontaneous fission also. The data on the spontaneous fission half-lives of 'No' are observed experimentally and the study on the spontaneous fission (SF)

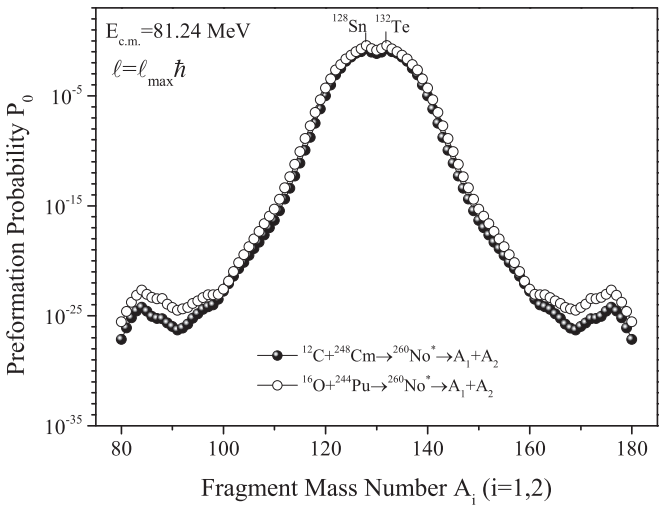

FIG. 12. The comparison of preformation probability distribution of compound nuclear system ^{260}No* considering two different incoming channels.

of No has been studied previously using the QMFT based preformed cluster model (PCM) (the ground state version of the DCM) in [69]. Here, an attempt is made to compare the preformation distributions of ^{260}No using the spontaneous fission and induced fission phenomena. Panel (a) of Fig. 13 presents the preformation probabilities for the ground state as well as excited state fission of ^{260}No, while considering the hot compact configuration of emitting fragments. It is seen that the mass distribution for all decay modes is almost the same for the hot deformed approach at both energies. It is to be noticed that the highest value of angular momentum is valid just for the induced decay mode of the ^{260}No compound nucleus. This result holds well in accordance with our previous study [70] on plutonium isotopes, where the structural profile of spontaneous and induced fission was investigated. Further, the role of orientations is investigated along with the deformation parameter. In panel (b) of this figure, the relevance of hot compact orientation is compared with the cold elongated configuration of decaying fragments at the highest compound nucleus energy having maximum value of angular momentum. The behavior of the fission fragments gets completely modified when we move from teh hot compact configuration to the cold elongated one. Whereas the hot configuration exhibits symmetric fragmentation, on the other hand, a purely asymmetric mass distribution is noticed in the case of a cold oriented configuration of emitting fragments.

Finally, the ground state fission of the ^{260}No nucleus is analyzed by using hot compact and cold elongated configurations of decaying fragments, so as to see the significance of orientations in the nuclear reactions. The comparison between the two approaches is presented in panel (c) of Fig. 13. It is concluded that there is a major difference in the preformation profile of ^{260}No for hot and cold approaches. The hot compact configuration exhibits a purely symmetric mass distribution, on the other hand, the cold deformed approach shows a purely asymmetric probability curve due to which the most probable fission fragments change. An almost similar behavior is seen for both spontaneous as well as induced fission cases by using the hot and cold oriented configurations. However, if we concentrate on the distinction between hot and cold orientations on the basis of the most probable emitting fragments, exactly the same fragments are found to be contributing in spontaneous as well induced fission phenomena for hot oriented configuration. The fragment having the highest probability is ^{128}Sn complementary to the ^{132}Te nucleus. On the other hand, in the case of the cold-elongated approach, nearby fragments are found to be contributing in the fission of ^{260}No. For the spontaneous fission case, these fragments are seen to be ^{102}Zr and ^{158}Sm, whereas the fragments change to ^{100}Zr and ^{160}Sm, while we consider the induced fission phenomenon. Thus, the above results indicate the importance of orientations along with the deformations of the emitting fragments.

Finally, to interpret the validity of DCM, the preformation distribution of the spontaneous fission of the ^{262}No nucleus calculated using the DCM is depicted in Fig. 14. This figure clearly shows that the mass distributions of the ^{262}No nucleus are purely symmetric and have nice agreement with the referred data [23]. Also, it is worth mentioning here that the fission mass distribution of heavy compound systems

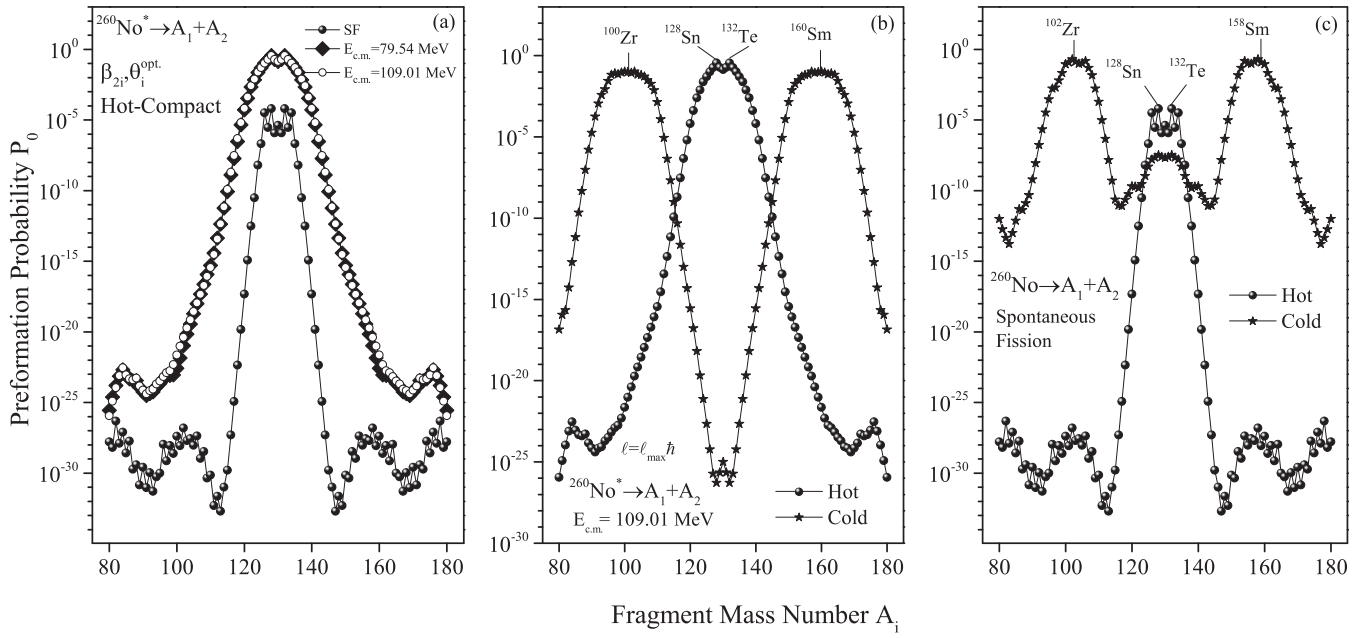

FIG. 13. Preformation distribution of $^{260}No^{*}$ showing the comparison of (a) spontaneous and induced fission (at extreme energies) using hot compact configuration, (b) hot-compact and cold elongated configuration of induced fission fragments, and (c) hot-compact and cold elongated configuration of spontaneous fission fragments.

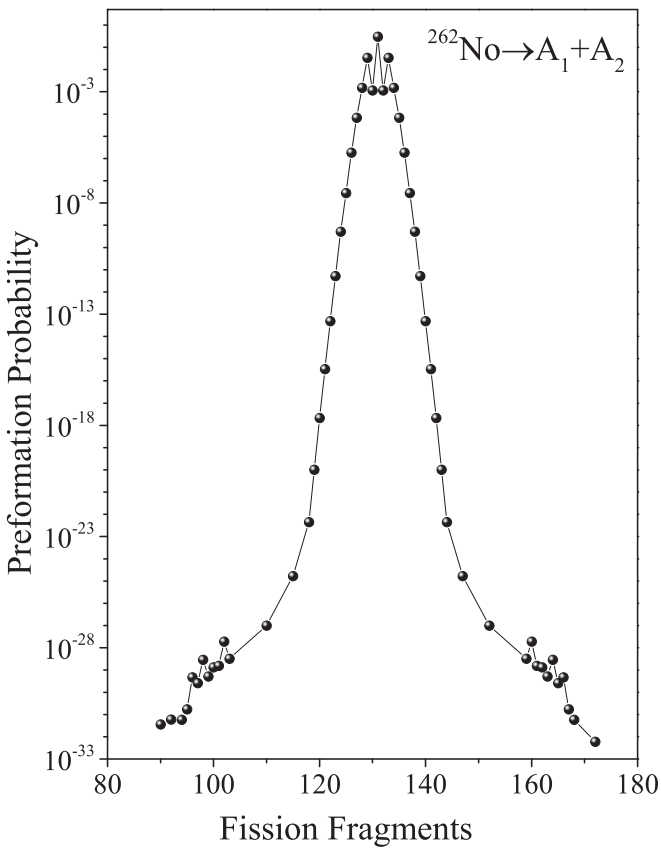

FIG. 14. DCM calculated preformation distribution of SF of the ^{262}No nucleus.

obtained using DCM has also been found in reasonable agreement with the available experimental mass distribution data in previously done work [33,70].

IV. SUMMARY

In the present analysis, we have examined the formation and decay of the $^{260}No^{*}$ nucleus. For fission analysis, theoretical calculations for $^{12}C+^{248}Cm$ and $^{16}O+^{244}Pu$ reactions have been done using the SAGBD model and Wong formula. As expected, the Wong formalism could not explain the fusion data in the sub-barrier region. This clearly suggests the importance of channel coupling effects in sub-barrier fusion dynamics. These effects enhance the fusion cross sections especially in the below barrier region and appropriately explain the fusion mechanism of studied reactions. In conjugation, the SAGBD approach intrinsically incorporates such effects and reasonably reproduces the experimental data. The effects of intrinsic degrees of freedom of participating nuclei have been quantitatively determined in terms of channel coupling parameter λ. The value of λ for $^{12}C+^{248}Cm$ and $^{16}O+^{244}Pu$ reactions has been found to have values of 2.53 and 3.18, respectively. In addition, reduced scale analysis has been done and more enhancements found for the $^{16}O+^{244}Pu$ over the $^{12}C+^{248}Cm$ reaction, which reflects the importance of entrance channel mass asymmetry effects. Thus, SAGBD calculations qualitatively and quantitatively reproduced the fusion mechanism of the studied reactions.

The coupled channel calculations are performed by using the coupled channel code CCFULL and in the coupled channel description. The impacts of inelastic surface excitations of

collision partners are considered explicitly. For both reactions, the inclusions of multiphonon vibrational states such as 2^+ and 3^- associated with the target isotopes are taken into account and found to play a very crucial role in the fusion dynamics of the given reactions. The couplings to the three phonon 2^+ and one phonon 3^- vibrational states of target isotopes in both reactions have turned out to be dominant for a complete description of the observed sub-barrier fusion enhancement. Furthermore, the couplings to projectile degrees of freedom in both reactions are additionally required to explain the fusion dynamics of studied systems and hence turned out to contribute significantly in the fusion process. The coupled channel outcome is not able to retrieve the sub-barrier fusion data of studied reactions without including the projectile degree of freedom. This clearly points towards the dominant impacts of projectile degrees of freedom as well as the multiphonon vibrational excitations of the target isotopes for an adequate description of the sub-barrier fusion enhancement of $^{12}C + ^{248}Cm$ and $^{16}O + ^{244}Pu$ reactions. The coupled channel calculations and the SAGBD calculations represents almost similar behavior of the given reactions but via different mathematical formulations and thus both approaches fairly explain the formation of compound nuclei via fusion channels.

Further, the fission analysis of the $^{260}No^*$ nucleus formed in $^{16}O + ^{244}Pu$ and $^{12}C + ^{248}Cm$ reactions is studied using the dynamical cluster decay model. The decay study is carried out at wide spread center-of-mass energies. The fission cross sections are calculated at all given energies and it is observed that the mass distribution of $^{260}No^*$ is nearly symmetric for compound nucleus fission. Further, at higher energies the diminishing of the fission barrier indicates the presence of some nCN process, which is in agreement with the referred experimental data. In view of this, the contribution of the nCN fission cross section ($\sigma_{\text{fission}}^{\text{nCN}}$) is also explored. The mass distribution of $\sigma_{\text{fission}}^{\text{nCN}}$ is asymmetric (unlike CN fission) and in agreement with experimental estimates. Finally, comparative analysis of the excited state and spontaneous fission is studied. Here, the role of orientations is comprehensively analyzed in view of the ground state as well as the excited state fission of the $^{260}No^*$ nucleus. The most probable fission fragments for both decay modes are observed to be identical.

ACKNOWLEDGMENTS

The author Vijay is sincerely thankful to Council of Scientific and Industrial Research (CSIR), New Delhi, India for providing a CSIR-JRF fellowship under Grant No. 09/1307(0001)/2020-EMR-I. N.G. acknowledges the financial support from Indian Institute of Technology, Ropar in the form of Post-Doctoral Fellowship.

[1] B. B. Back, H. Esbensen, C. L. Jiang, and K. E. Rehm, Rev. Mod. Phys. **86**, 317 (2014).
[2] G. Montagnoli and A. M. Stefanini, Eur. Phys. J. A **53**, 169 (2017).
[3] M. S. Gautam, A. Kaur, and M. K. Sharma, Phys. Rev. C **92**, 054605 (2015).
[4] A. B. Balantekin and N. Takigawa, Rev. Mod. Phys. **70**, 77 (1998).
[5] M. Dasgupta, D. J. Hinde, N. Rowley, and A. M. Stefanini, Annu. Rev. Nucl. Part. Sci. **48**, 401 (1998).
[6] M. S. Gautam, Vijay, R. P. Chahal, H. Khatri, and S. Duhan, AIP Conf. Proc. **2352**, 50019 (2021).
[7] M. S. Gautam, S. Duhan, R. P. Chahal, H. Khatri, S. B. Kuhar, and K. Vinod, Phys. Rev. C **102**, 014614 (2020).
[8] R. G. Stokstad, Y. Eisen, S. Kaplanis, D. Pelte, U. Smilansky, and I. Tserruya, Phys. Rev. Lett. **41**, 465 (1978).
[9] M. S. Gautam, H. Khatri, and K. Vinod, Int. J. Mod. Phys. E **28**, 1950006 (2019).
[10] M. Singh, Sukhvinder, and R. Kharab, Mod. Phys. Lett. A **26**, 2129 (2011).
[11] M. Singh, Sukhvinder, and R. Kharab, Nucl. Phys. A **897**, 179 (2013).
[12] M. Dasgupta, A. Navin, Y. K. Agarwal, C. V. K. Baba, H. C. Jain, M. L. Jhingan, and A. Roy, Nucl. Phys. A **539**, 351 (1992).
[13] J. O. Newton, R. D. Butt, M. Dasgupta, D. J. Hinde, I. I. Gontchar, C. R. Morton, and K. Hagino, Phys. Rev. C **70**, 024605 (2004).
[14] N. Rowley, G. R. Satchler, and P. H. Stelson, Phys. Lett. B **254**, 25 (1991).
[15] E. F. Aguilera, J. J. Kolata, and R. J. Tighe, Phys. Rev. C **52**, 3103 (1995).
[16] V. Zanganeh, R. Gharaei, and A. M. Izadpanah, Nucl. Phys. A **992**, 121637 (2019).
[17] E. Piasecki, M. Kowalczyk, S. Yusa, A. Trzcinska, and K. Hagino, Phys. Rev. C **100**, 014616 (2019).
[18] E. F. Aguilera, J. J. Vega, J. J. Kolata, A. Morsad, R. G. Tighe, and X. J. Kong, Phys. Rev. C **41**, 910 (1990).
[19] M. S. Gautam, Chinese Journal of Physics **54**, 86 (2016).
[20] M. S. Gautam, K. Vinod, and H. Kumar, Nucl. Phys. A **984**, 9 (2019).
[21] M. Ismail, W. M. Seif, and E. El-Gebaly, Phys. Lett. B **563**, 53 (2003).
[22] M. S. Gautam, Phys. Rev. C **90**, 024620 (2014).
[23] T. Banerjee *et al.*, Phys. Rev. C **102**, 024603 (2020).
[24] Vijay, R. P. Chahal, M. S. Gautam, S. Duhan, and H. Khatri, Phys. Rev. C **103**, 024607 (2021).
[25] K. Hagino, N. Rowley, and A. T. Kruppa, Comput. Phys. Commun. **123**, 143 (1999).
[26] N. Grover, G. Kaur, and M. K. Sharma, Phys. Rev. C **93**, 014603 (2016).
[27] G. Kaur, K. Sandhu, and M. K. Sharma, Phys. Rev. C **94**, 014615 (2016).
[28] A. Kaur, G. Kaur, and M. K. Sharma, Nucl. Phys. A **941**, 152 (2015).
[29] G. Sawhney, A. Kaur, M. K. Sharma, and R. K. Gupta, Phys. Rev. C **92**, 064303 (2015).
[30] G. Kaur and M. K. Sharma, Phys. Rev. C **87**, 044601 (2013).
[31] G. Kaur and M. K. Sharma, Nucl. Phys. A **884–885**, 36 (2012).
[32] G. Sawhney, G. Kaur, M. K. Sharma, and R. K. Gupta, Phys. Rev. C **88**, 034603 (2013).
[33] S. Kumar, N. Kumar, S. Mandal, S. C. Pancholi, P. C. Srivastava, A. K. Jain, R. Palit, S. Saha, J. Sethi, B. S. Naidu,

R. Donthi, P. K. Joshi, T. Trivedi, S. Muralithar, R. P. Singh, R. Kumar, A. Dhal, and R. K. Bhowmik, Phys. Rev. C **90**, 024315 (2014).
[34] M. Kaur and M. K. Sharma, Eur. Phys. J. A **50**, 61 (2014).
[35] H. J. Fink, J. Maruhn, W. Scheid, and, W. Greiner, Z. Phys. **268**, 321 (1974).
[36] J. Maruhn and W. Greiner, Phys. Rev. Lett. **32**, 548 (1974).
[37] R. K. Gupta, W. Scheid, and W. Greiner, Phys. Rev. Lett. **35**, 353 (1975).
[38] B. B. Singh, M. K. Sharma, and R. K. Gupta, Phys. Rev. C **77**, 054613 (2008).
[39] S. J. Sanders *et al.*, Phys. Rev. C **41**, R1901(R) (1990).
[40] D. J. Hinde, R. du Rietz, M. Dasgupta, R. G. Thomas, and L. R. Gasques, Phys. Rev. Lett. **101**, 092701 (2008).
[41] R. du Rietz, D. J. Hinde, M. Dasgupta, R. G. Thomas, L. R. Gasques, M. Evers, N. Lobanov, and A. Wakhle, Phys. Rev. Lett. **106**, 052701 (2011).
[42] W. Q. Shen *et al.*, Phys. Rev. C **36**, 115 (1987).
[43] Y. Aritomo and M. Ohta, Nucl. Phys. A **753**, 152 (2005).
[44] B. B. Back *et al.*, Phys. Rev. C **32**, 195 (1985).
[45] A. C. Berriman, D. J. Hinde, M. Dasgupta, C. R. Morton, R. D. Butt, and J. O. Newton, Nature (London) **413**, 144 (2001).
[46] J. Khuyagbaatar *et al.*, Eur. Phys. J. A **46**, 59 (2010)
[47] D. J. Hinde, M. Dasgupta, J. R. Leigh, J. C. Mein, C. R. Morton, J. O. Newton, and H. Timmers, Phys. Rev. C **53**, 1290 (1996).
[48] J. C. Mein, D. J. Hinde, M. Dasgupta, J. R. Leigh, J. O. Newton, and H. Timmers, Phys. Rev. C **55**, R995(R) (1997).
[49] K. Nishio *et al.*, Nucl. Data Sheets **119**, 299 (2014).
[50] C. Ngô, C. Gregoire, B. Remaud, and E. Tomasi, Nucl. Phys. A **400**, 259 (1983).
[51] B. B. Back, J. Phys.: Conf. Ser. **282**, 012003 (2011).
[52] D. M. Brink and U. Smilansky, Nucl. Phys. A **405**, 301 (1983).
[53] D. L. Hill and J. A. Wheeler, Phys. Rev. **89**, 1102 (1953).
[54] C. Y. Wong, Phys. Rev. Lett. **31**, 766 (1973).
[55] P. H. Stelson, Phys. Lett. B **205**, 190 (1988).
[56] K. Siwek-Wilczyńska and J. Wilczyński, Phys. Rev. C **69**, 024611 (2004).
[57] K. Hagino and N. Takigawa, Prog. Theor. Phys. **128**, 1061 (2012).
[58] H. Kroger and W. Scheid, J. Phys. G: Nucl. Phys. **6**, L85 (1980).
[59] N. J. Davidson *et al.*, Nucl. Phys. A **570**, 61 (1994).
[60] G. Audi, A. H. Wapstra, and C. Thiboult, Nucl. Phys. A **729**, 337 (2003).
[61] G. Audi and A. H. Wapstra, Nucl. Phys. A **595**, 409 (1995).
[62] W. Myers and W. J. Swiatecki, Nucl. Phys. **81**, 1 (1966).
[63] G. Royer and J. Mignen, J. Phys. G: Nucl. Part. Phys. **18**, 1781 (1992).
[64] A. Kaur and M. K. Sharma, Phys. Rev. C **99**, 044611 (2019).
[65] Vijay, R. P. Chahal, M. S. Gautam, S. Duhan, and H. Khatri, Int. J. Mod. Phys. E **30**, 2150075 (2021).
[66] B. Pritychenko, M. Birch, B. Singh, and M. Horoi, At. Data Nucl. Data Tables **107**, 1 (2016).
[67] T. Kibedi and R. H. Spear, At. Data Nucl. Data Tables **80**, 35 (2002).
[68] S. S. Kapoor and V. Ramamurthy, Pramana - J. Phys. **33**, 161 (1989)
[69] K. Sharma, G. Sawhney, and M. K. Sharma, Phys. Rev. C **96**, 054307 (2017).
[70] K. Sharma, G. Sawhney, M. K. Sharma, and Raj K. Gupta, Nucl. Phys. A **972**, 1 (2018).